OXFORD

Human Molecular Genetics, 2023, Vol. 32, 16, 2587–2599
https://doi.org/10.1093/hmg/ddad085
Advance access publication date 25 May 2023
Original Article

Reticulons 1 and 3 are essential for axonal growth and synaptic maintenance associated with intellectual development

John Zhou[1,2], Qi Shi[2], Ying Y. Ge[1,2], Wanxia He[1,2], Xiangyou Hu[1,2], Weiming Xia[3,4,5] and Riqiang Yan[1,2,*]

[1]Department of Neuroscience, UConn Health, 263 Farmington Avenue, Farmington, CT 06030-3401, USA
[2]Department of Neuroscience, Cleveland Clinic Lerner Research Institute, 9500 Euclid Avenue, Cleveland, OH 44195, USA
[3]Pharmacology & Experimental Therapeutics, Boston University, 72 E Concord St, Boston, MA 02118, USA
[4]Geriatric Research Education and Clinical Center, Bedford VA Healthcare System, Bedford, MA 01730, USA
[5]Biological Sciences, Kennedy College of Science, University of Massachusetts Lowell, Lowell, MA 01854, USA

*To whom correspondence should be addressed. Tel: 8606793527; Fax: 860-679-8766; Email: riyan@uchc.edu

Abstract

Reticulon (RTN) proteins are a family of proteins biochemically identified for shaping tubular endoplasmic reticulum, a subcellular structure important for vesicular transport and cell-to-cell communication. In our recent study of mice with knockout of both reticulon 1 (*Rtn1*) and *Rtn3*, we discovered that *Rtn1*$^{-/-}$;*Rtn3*$^{-/-}$ (brief as R1R3dKO) mice exhibited neonatal lethality, despite the fact that mice deficient in either RTN1 or RTN3 alone exhibit no discernible phenotypes. This has been the first case to find early lethality in animals with deletion of partial members of RTN proteins. The complete penetrance for neonatal lethality can be attributed to multiple defects including the impaired neuromuscular junction found in the diaphragm. We also observed significantly impaired axonal growth in a regional-specific manner, detected by immunohistochemical staining with antibodies to neurofilament light chain and neurofilament medium chain. Ultrastructural examination by electron microscopy revealed a significant reduction in synaptic active zone length in the hippocampus. Mechanistic exploration by unbiased proteomic assays revealed reduction of proteins such as FMR1, Staufen2, Cyfip1, Cullin-4B and PDE2a, which are known components in the fragile X mental retardation pathway. Together, our results reveal that RTN1 and RTN3 are required to orchestrate neurofilament organization and intact synaptic structure of the central nervous system.

Introduction

The prototypic cellular function of the reticulon (RTN) protein family is to shape the tubular endoplasmic reticulum (ER) (1). The tubular ER network is part of the smooth ER and comprises membranes with high curvature. Functionally, the tubular ER may mediate vesicle transport, organelle contacts and cellular communications (2–4). This function of RTN family is evolutionarily conserved (5,6). In *Saccharomyces cerevisiae*, two *rtn* genes are present in its genome. Yeast cells with both *rtn* genes knocked out are normal, but deletion of an additional tubular ER protein REEP/Yop gene disrupts the tubular ER (7), indicating the overlapping function of RTN and REEP family proteins. Drosophila have only one functional *rtn* gene (*Rtnl1*), and its deletion is viable, although noted expansion of epidermal ER sheets, and partial loss of smooth ER markers from distal but not proximal motor axons occurs in an age-dependent manner (8). Deletion of drosophila *Rtnl1* and *REEP* family members results in additionally disrupted smooth ER integrity such as a reduced network with fewer and larger tubules and occasional gaps in the network (9).

Mammalian RTN family has four members (RTN1-RTN4) with distinct expression profiles and functions (10,11). Mutations in RTN2 are linked to the pathogenesis of hereditary spastic paraplegia (12), a disease with notable axonal degeneration. RTN4 (also known as Nogo-A) was initially discovered as a potent inhibitor of neurite outgrowth (13,14). Mice with deficiency in Nogo (RTN4) displayed defects in neurite outgrowth (15), vascular remodeling (16) and liver regeneration (17).

Our interests in RTN proteins dated back to our initial discovery of RTNs interaction with Alzheimer's β-secretase, also known as BACE1 (18), mainly through its conserved C-terminal residues (19). Mouse genetic studies reveal that RTN3, but not other RTN family members, is abnormally accumulated in the dystrophic neurites that are usually found in surrounding amyloid plaques (20,21) and regulates amyloid deposition in mouse models (22). Both RTN3 and RTN1 are abundantly expressed in neurons, whereas RTN2 and 4 are weakly expressed in neuronal cells in the rodent brain (21). Singular deletion of *Rtn1* or *Rtn3* results in no obviously discernible abnormality in the mouse development (21). Notably, RTN1 and RTN3 protein levels appear to be compensatory (21), suggesting some functional overlap between these two proteins.

This observation motivated us to create Rtn1 and Rtn3 double knockout, *Rtn1*$^{-/-}$;*Rtn3*$^{-/-}$ (distinctly briefed as R1R3dKO) mice to examine the function of these two potentially compensatory RTN proteins through phenotypic analyses. Surprisingly, R1R3dKO mice were unable to survive beyond postnatal day 1 (P1), without manual feeding. Bungarotoxin staining of the acetylcholine receptor (AChR) in R1R3dKO diaphragms revealed significantly disrupted AChR distribution at the phrenic nerve end plates. This

Received: March 21, 2023. **Revised:** April 25, 2023. **Accepted:** April 29, 2023

disruption most likely resulted in respiratory distress, contributing to early lethality of these R1R3dKO mice. Analyses of embryonic and neonatal R1R3dKO brains revealed striking and specific loss of neurofilament light and medium chain (NFL and NFM) staining in the rostral hippocampal stratum lacunosum moleculare (SLM) and angular bundle along the temporammonic pathway. Overall sheet and tubular ER morphology in the hippocampus was not obviously altered by ultrastructural examination, but reduction of active zone length at the SLM of R1R3dKO brains was noted. A mechanistic study by unbiased proteomic analysis unveiled several significantly downregulated proteins, which are known to control synaptic homeostasis and intellectual development. Altogether, our study demonstrates that rodent RTN1 and RTN3 are highly important for mouse survival and appear to jointly play a critical role in mammalian axonal cytoskeleton arrangement and synaptic maintenance.

Results

Deletion of both *Rtn1* and *Rtn3* causes neonatal lethality

We have previously reported that mice with singular deletion of either *Rtn1* (21) or *Rtn3* (22) are viable and have no obviously discernible growth abnormality. No abnormality of tubular ER structure was observed in these two KO models. Although RTN3 is ubiquitously expressed, it is most richly expressed in neurons (22). RTN1 is more restrictively expressed in the embryonic and neonatal brains, validated by neuronal cells using KO samples with our antibody R418 (21). Furthermore, *Rtn3* KO mice have a small increase in RTN1 protein levels, suggesting a compensatory and functional overlap between these two proteins (21).

To examine the possible joint function of RTN1 and RTN3, we generated $Rtn1^{-/-};Rtn3^{-/-}$ (R1R3dKO) mice through breeding $Rtn1^{+/-};Rtn3^{+/-}$ with $Rtn1^{+/-};Rtn3^{+/-}$ *mice*. This breeding strategy resulted in eight genotypes, including R1R3dKO (Fig. 1A). Among 1,272 documented pups produced from this mating strategy, we found that almost all R1R3dKO mice could not survive beyond 24 h [The first 24 h after birth were designated as postnatal day 0 (P0)], and this early lethality had no sex discrimination. If given special care, such as the manual feeding of glucose water to neonates after the birth, four pups were survived up to P9 (Fig. 1A). In the embryonic stage, the expected Mendelian ratios were observed. We also noted that R1R3dKO embryos showed no difference in body size or gross appearance from E14 to E18 compared with other genotype littermates, indicating the lethality occurred after the birth. A noted reduction of neonatal survival was also seen in $Rtn1^{-/-};Rtn3^{+/-}$ (123/147) and $Rtn1^{+/-};Rtn3^{-/-}$ (120/146). This suggests that just one copy of *Rtn1* or *Rtn3* might offer limited protection. Since the similar survival rate and developmental appearance among $Rtn1^{+/+};Rtn3^{+/+}$, $Rtn1^{+/+};Rtn3^{+/-}$, $Rtn1^{+/+};Rtn3^{-/-}$, $Rtn1^{+/-};Rtn3^{+/+}$, $Rtn1^{+/-};Rtn3^{+/-}$, $Rtn1^{-/-};Rtn3^{+/+}$ pups were similar, these mice were grouped to be control littermates (Ctrl) for phenotypic comparisons, but genotypes of the individual sample for this group were marked in the study.

As aforementioned, four R1R3dKO pups survived past P1 (P3, P7, P8 and P9) via handfeeding of glucose containing water. In our observation, newborn R1R3dKO neonates were initially indistinguishable from their littermates, but R1R3dKO experienced defects in growth after P0 (Fig. 1B). Even with additional care, no R1R3dKO mice survived beyond P9.

To identify the causal factors for the lethality, we conducted histological examinations of all organs. Via hematoxylin and eosin (H & E) staining, we noted congested alveolar air spaces in the P0 R1R3dKO lung, unlike that in Ctrl littermates (Fig. 1C). We then examined acetylcholine esterase receptor (AChR) localization in the diaphragm of R1R3dKO and control mice via α-bungarotoxin staining. As shown in Figure 1D, AChR in the R1R3dKO diaphragm was visibly disorganized from the normal laminar distribution at the phrenic nerve end plate area. Quantification of AChR puncta within this phrenic nerve end plate area confirmed a significant reduction of AChR puncta area in R1R3dKO compared with controls (Fig. 1E). This observation suggests that oxygen exchange was weakened in the R1R3dKO lung, and this could exacerbate neonatal respiratory distress and contribute to neonatal lethality.

Rtn1 and *Rtn3* dual deficiency alters the cytoskeleton organization in axons

When examining R1R3dKO mouse brains by Nissl staining, we noticed that P0 R1R3dKO mouse brains were not different in their gross appearances compared with Ctrl littermates (Supplementary Material, Fig. S1). However, histological staining with various antibodies to neurites revealed remarkable differences. Neurofilament light chain (NFL)-labeled axons were missing in the rostral portions of the SLM and angular bundle in P0 R1R3dKO pups compared with control littermates (Fig. 2A and Supplementary Material, Fig. S2A). This was further confirmed with antibody to neurofilament medium chain (NFM) (Fig. 2B) and SMI31 (Fig. 2C and Supplementary Material, Fig. S2B), which recognizes the extensively phosphorylated neurofilament heavy chain (NFH) and NFM. This axonal staining deficit was the most evident in coronal sections, ∼+3.87 mm from anterior pole (Fig. 2D). A slight reduction in NFL staining of the fimbria of the fornix was also noticed in sections (arrows in Fig. 2A and D). The SLM and angular bundle form portions of the temporammonic pathway with origins in neuronal bodies beginning in the entorhinal cortex layer II. The fimbria is a white matter region that originates in hippocampal regions and projects to mammillary bodies and the rest of the limbic system.

Interestingly, the NFL expression in SLM and angular bundle from coronal sections distal to 5.07 mm from anterior pole and more proximal to the entorhinal cortex appeared to be unchanged (Fig. 2D). Thus, only distal portions of the temporammonic pathway in R1R3dKO at P0 appear to be affected. Serial sagittal sectioning confirmed progressive decrease in the NFL expression in more distal portions of temporammonic pathway in P0 R1R3dKO pups (Fig. 2E and F, also see Supplementary Material, Fig. S2A and Supplementary Material, Video S1). We also stained P0 brain sections with MAP2 antibody and did not detect obvious defects (Supplementary Material, Fig. S2C). Hence, the axonal structure in the hippocampal and limbic system was partially impaired in R1R3dKO mouse brains. This impairment could track back to embryonic E17 as lack of NFL-labeled axons was already observed in the cortex, angular bundle, CA1 SLM and subiculum of R1R3dKO embryos (Fig. 3).

Defect in axonal growth was more evident in R1R3dKO mice survived beyond P0. In the case of a P8 R1R3dKO mouse, axonal aberration was striking, with prominent loss of NFL expression in axon collaterals of the striatum lacunosum and angular and the outer layer of the dentate gyrus (Fig. 4A). The same regional loss of NFL expression in the hippocampus was also evident in P7 R1R3dKO mice (Supplementary Material, Fig. S3). This reflected an impaired perforant pathway, which is a cortical to hippocampal projection originating in layer III entorhinal cortex and forms synapses along the outer portion of the molecular layer of the dentate gyrus. The significant loss of NFL expression in the fornix and the mammillothalamic tract (Fig. 4B) was also observed. The fornix is another part of the limbic system that projects signals between the hippocampus and mammillary bodies through the

A

Genotype	*Rtn1*$^{+/+}$; *Rtn3*$^{+/+}$	*Rtn1*+/+; *Rtn3*+/-	*Rtn1*$^{+/+}$; *Rtn3*$^{-/-}$	*Rtn1*$^{+/-}$; *Rtn3*$^{+/+}$	*Rtn1*$^{+/-}$; *Rtn3*$^{+/-}$	*Rtn1*$^{+/-}$; *Rtn3*$^{-/-}$	*Rtn1*$^{-/-}$; *Rtn3*$^{+/+}$	*Rtn1*$^{-/-}$; *Rtn3*$^{+/-}$	*Rtn1*$^{-/-}$; *Rtn3*$^{-/-}$
Mendelian ratio	1/16	1/8	1/16	1/8	1/4	1/8	1/16	1/8	1/16
Expected births (n = 1,272 pups)	79.3125	158.625	79.3125	158.625	317.25	158.625	79.3125	158.625	79.3125
Live births	87	174	75	168	303	147	81	146	90
P0 survival	87	171	72	168	303	123	78	120	4

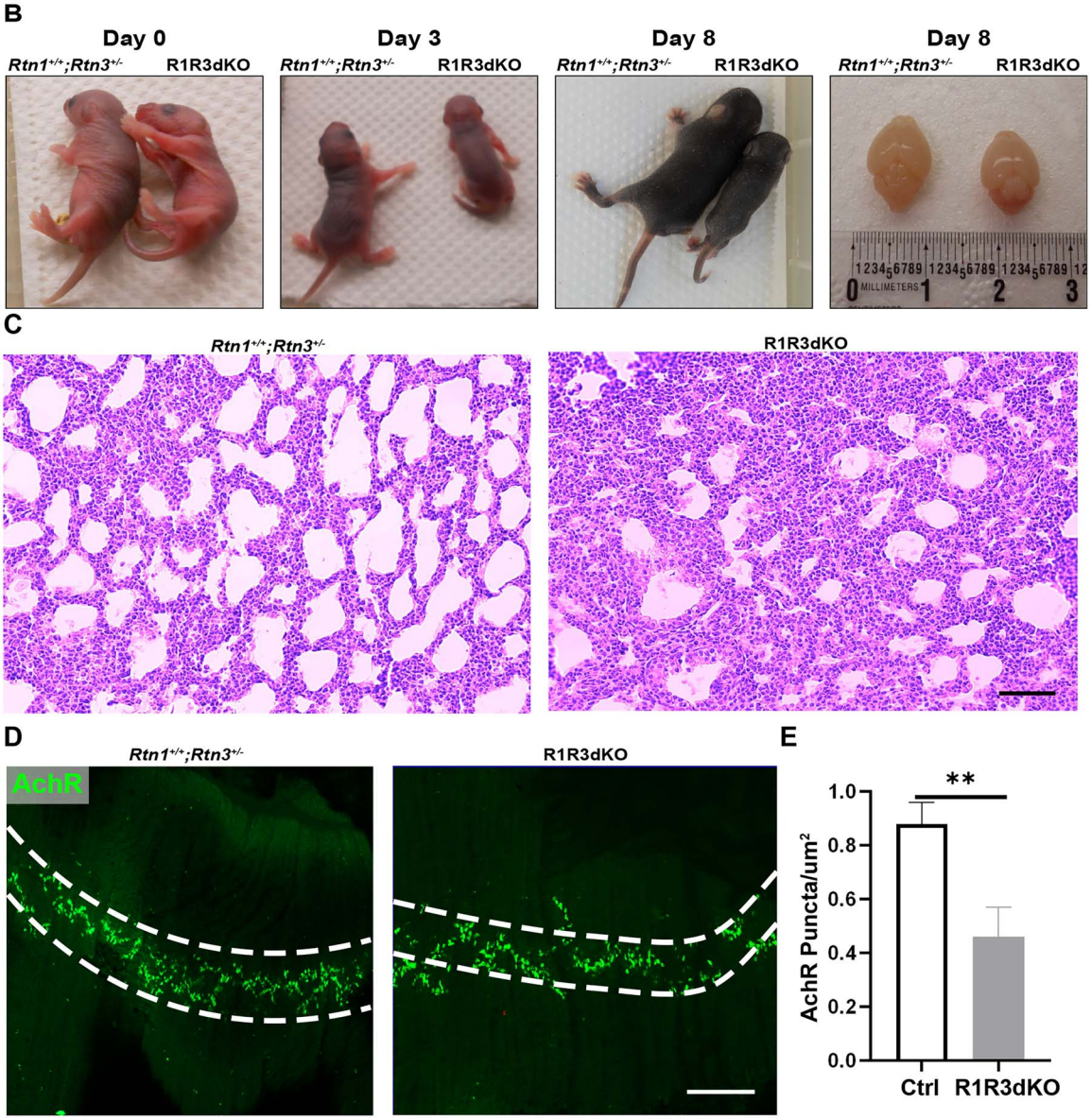

Figure 1. Dual deletion of *Rtn1* and *Rtn3* results in neonatal lethality and delayed growth. (**A**) Birth information of 1,272 mice pups resulting from *Rtn1*$^{+/-}$;*Rtn3*$^{+/-}$ X *Rtn1*$^{+/-}$;*Rtn3*$^{+/-}$. Statistics include expected births according to the Mendelian ratio, actual live births and total survival after P0, were recorded for each resulting genotype. Only 4 of 90 R1R3dKO mouse pups survived past P0. (**B**) A R1R3dKO mouse that survived to P8 feeding with glucose-containing water was noticeably smaller than compared with a *Rtn1*$^{+/+}$;*Rtn3*$^{+/-}$ littermate beginning at P3. Brain size of R1R3dKO mouse was also much smaller at P8. (**C**) Representative H & E staining of lungs from P0 R1R3dKO mice and *Rtn1*$^{+/+}$; *Rtn3*$^{+/-}$ littermates reveal alveolar congestion pathology. Scale bar, 200 μm. (**D**) Bungarotoxin staining of AChR in P0 R1R3dKO and *Rtn1*$^{+/+}$;*Rtn3*$^{+/-}$ littermate diaphragm revealed disorganization of AChR localization and neuromuscular junction. White dotted lines indicate area for phrenic nerve endplates. Scale bar, 100 μm. (**E**) Quantification of instances of Bungarotoxin-positive puncta within normalized area (in μm^2) for phrenic nerve endplates from P0 R1R3dKO mice and Ctrl littermates. Significant reduction in correct localization of AChR puncta to phrenic nerve endplates was observed in P0 R1R3dKO mice ($n = 3$ for each group, Student's *t*-test, ** indicates *P*-value < 0.01).

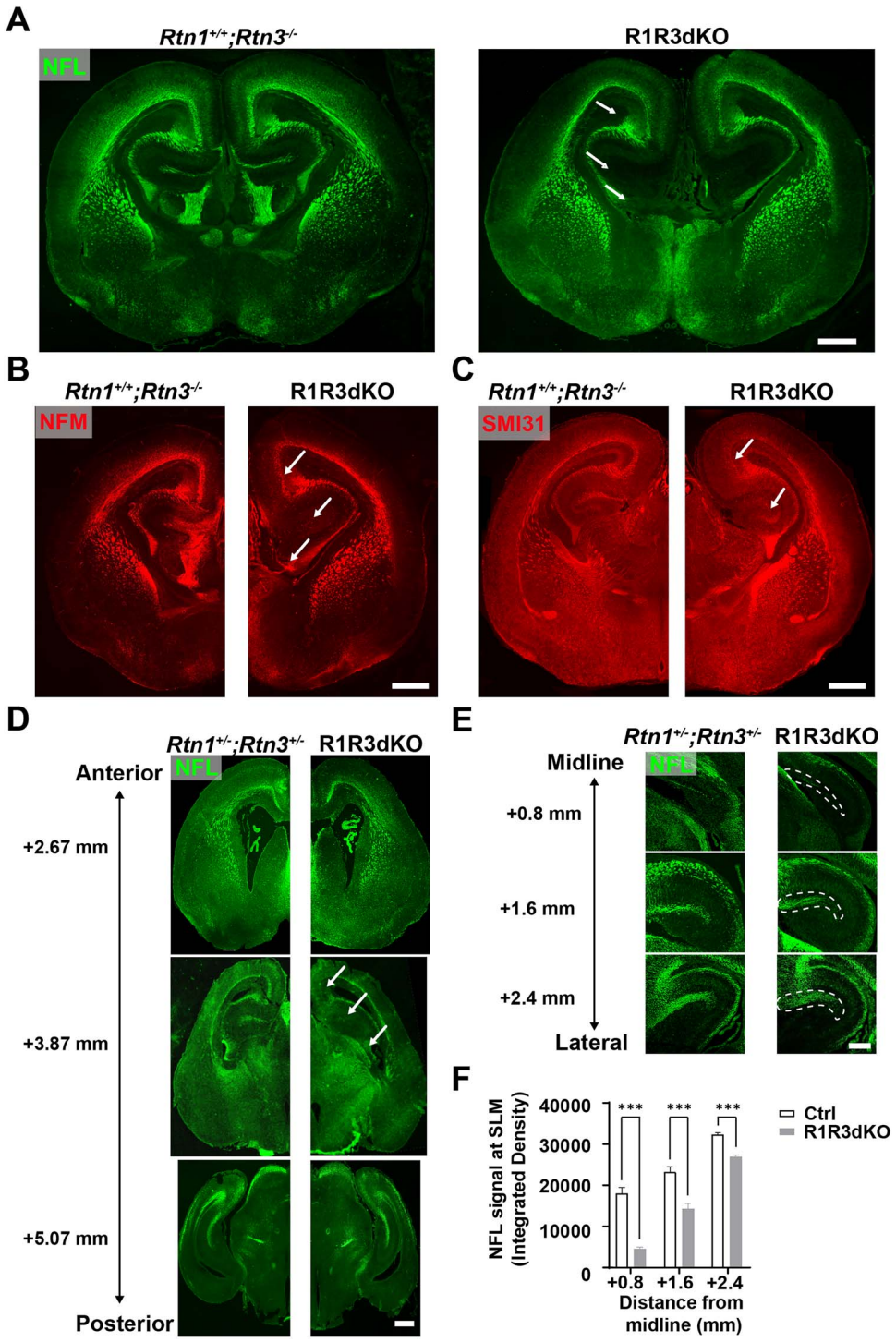

Figure 2. *Rtn1* and *Rtn3* dual deficiency alters axonal projection. Representative images of NFL (**A**), NFM (**B**) and SMI31 (**C**) staining of coronal brain sections from P0 R1R3dKO and $Rtn1^{+/+};Rtn3^{-/-}$ littermates. White arrows indicate missing axon cytoskeleton elements in the SLM, angular bundle and fornix of R1R3dKO pups. Scale bar, 500 μm. (**D**) Serial sectioning and NFL staining of coronally sectioned brains from P0 R1R3dKO and $Rtn1^{+/-};Rtn3^{+/-}$ littermates. Images are arranged from anterior to posterior pole and labeled according to comparable sections +2.67, 3.87 and 5.07 mm from anterior pole in the mouse brain atlas. White arrows indicate missing NFL expression in the SLM, angular bundle and fornix of R1R3dKO pups, noticeable at +3.87 mm from the anterior pole. Scale bar, 500 μm. (**E**) NFL staining of sagittal brain sections from P0 R1R3dKO and $Rtn1^{+/-}$; $Rtn3^{+/-}$ littermates. Images are arranged from medial to lateral directions and labeled according to comparable sections +0.8, 1.6 and 2.4 mm from midline. White dotted outlines indicate SLM. NFL immunity is reduced in the SLM, with progressive decline occurring in more midline sections, distal to the entorhinal cortex. Scale bar, 200 μm. (**F**) Quantification of raw integrated fluorescent NFL intensity in the SLM boundaries from P0 R1R3dKO and Ctrl littermates. Sections that were +0.8, 1.6 and 2.4 mm from midline were chosen for quantification ($n = 6$, two-way ANOVA with Sidak post test comparison between genotypes, *** indicates P-value < 0.001).

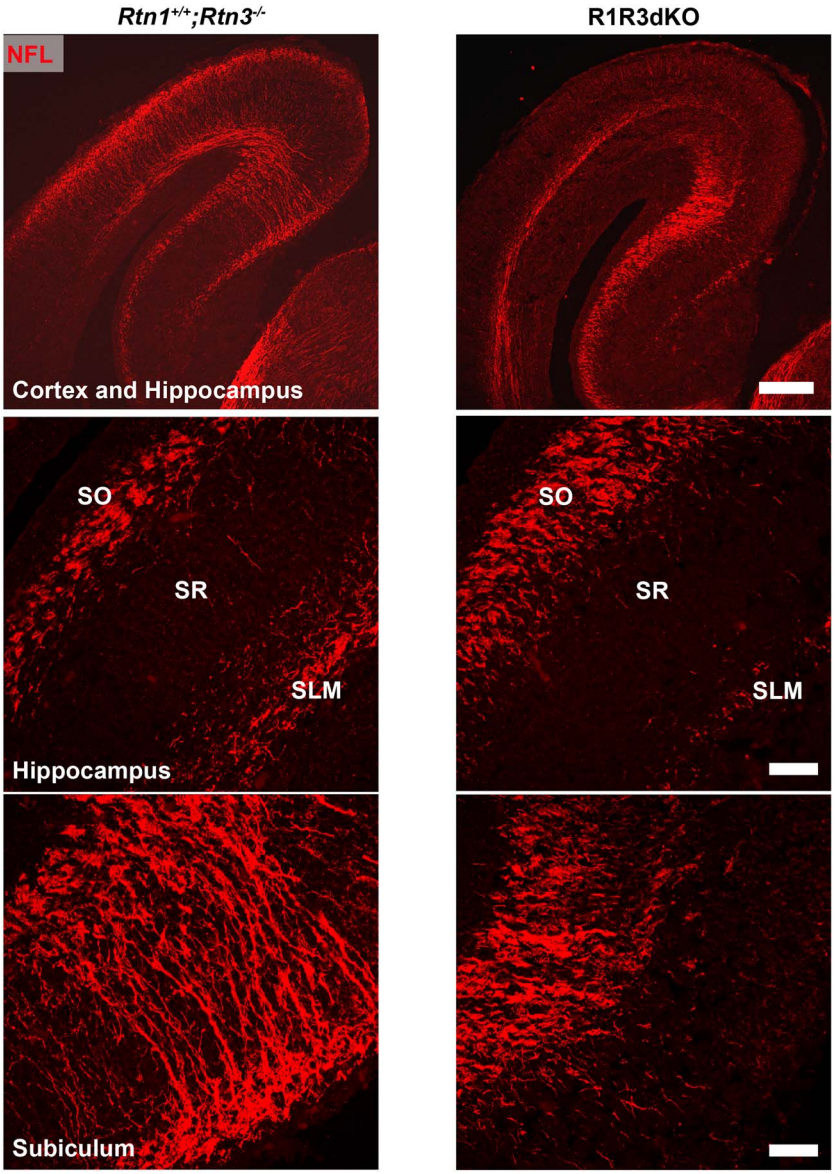

Figure 3. Axonal projection deficits are noted in *Rtn1* and *Rtn3* dual deficient embryos. Representative images of the NFL signal from E17 R1R3dKO and *Rtn1*$^{+/+}$; *Rtn3*$^{-/-}$ littermates from the cortex and hippocampus (scale bar, 200 μm) exhibited reduction across cortical regions, angular bundle, subiculum and SLM. Magnified images of CA1 hippocampus stratum oriens (SO), stratum radiatum (SR) and SLM show severe reduction in NFL immunity at the SLM and angular bundle fibers (scale bar 50 um) in R1R3dKO day 17 (E17) embryos.

hypothalamus and was similarly reduced. The mammillothalamic tract, part of the diencephalon region of the limbic system, is important for recollective and spatial memory and was also significantly reduced. Because NFL expression in the fornix and mammillothalamic tract of P0 R1R3dKO mouse brains was not obviously altered, we infer that axonal degeneration will become more deteriorated in R1R3dKO mice if grown beyond P0. Consistent with this, axons in the cortical layers showed loss of NFL staining in this P8 R1R3dKO mouse brain and neuronal nuclei appeared to be less dense (Fig. 4C). Moreover, CA1 pyramidal neurons were smaller and compacted (Fig. 4D). Despite this, dendritic morphology stained by MAP2 in CA1 appeared to be unchanged between R1R3dKO and Ctrl mice (Fig. 4D). We also noted marginal difference between P0 R1R3dKO and Ctrl neonates, marked by NeuN staining (Supplementary Material, Fig. S4A) or cell proliferation marker Ki67 staining (Supplementary Material, Fig. S4B).

While the overall brain size in P8 R1R3dKO mice was reduced (Fig. 1B), the brain size of P0 R1R3dKO mice was not different from littermates. We showed that distribution of Cajal–Retzius cells that form axonal guideposts for the SLM, stained by antibody to Reelin or P73 (known as Tumor Protein P73), was not obviously altered (Supplementary Material, Fig. S4C and D). Altogether, our results indicate that deficiency in mouse RTN1 and RTN3 results in defects in axonal growth, most prominently in the distal portions of the temporammonic, perforant and limbic pathways. This defect will become more discernable with mice that live beyond P0.

Rtn1 and *Rtn3* dual deficiency shows no obvious alteration in tubular ER morphology but reduces active zone length in SLM

Since RTN proteins are known to shape tubular ER, we then examined whether axonal defects, especially in SLM, are related to disrupted electronic microscopic (EM) structure. We also performed reverse osmium tetraoxide (rOTO) EM staining to enhance plasma membrane contrast in SLM axons according to the published procedure (23). By comparing multiple hippocampal and cortical samples, we found no distinct differences in morphology

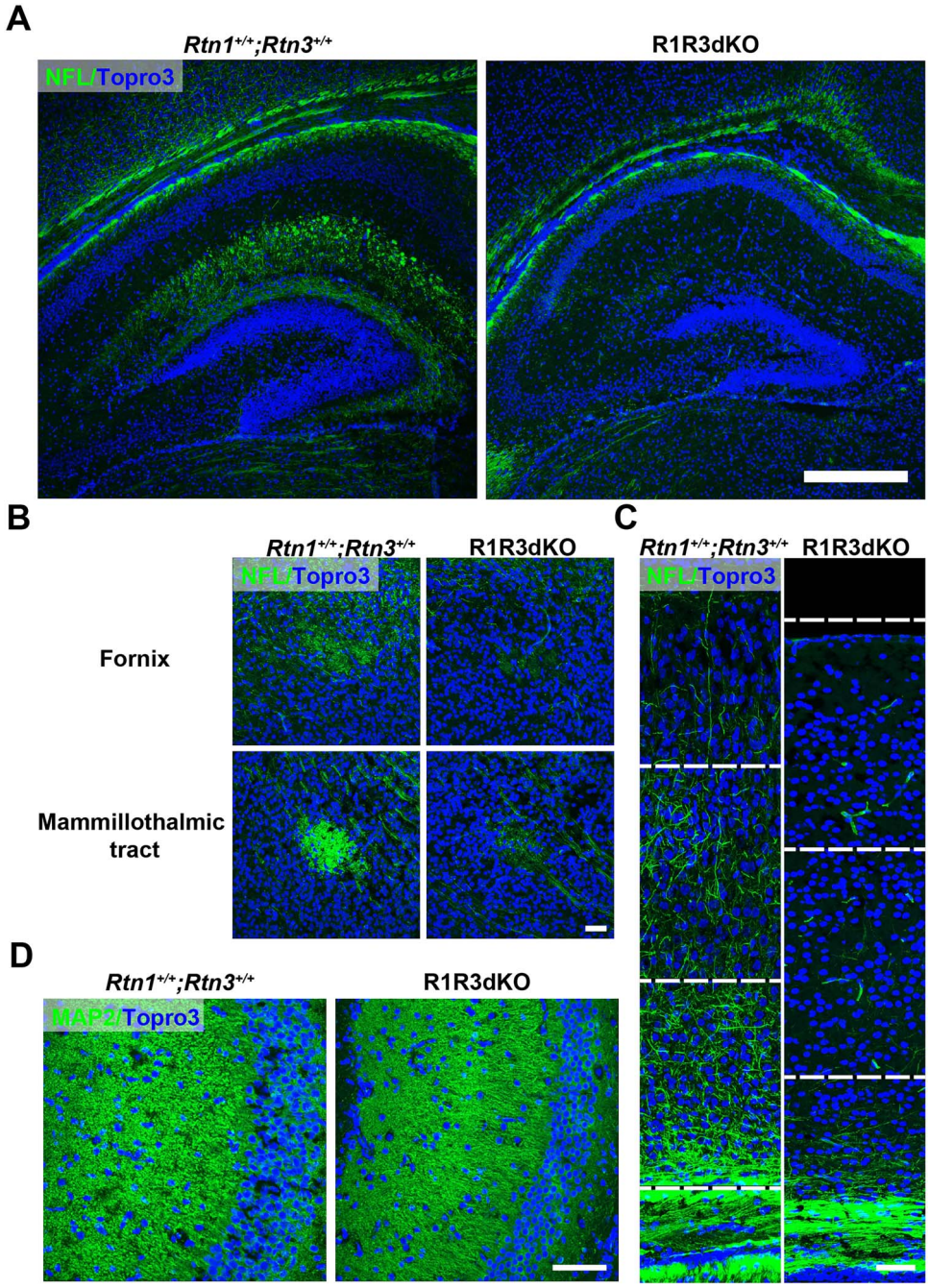

Figure 4. Striking axonal deficits in neonatal *Rtn1* and *Rtn3* dual deficiency. (**A**) Loss of NFL expression in P8 R1R3dKO coronal brain sections is noted in all areas of the hippocampus compared with $Rtn1^{+/+}$; $Rtn3^{+/+}$ littermate. Scale bar, 500 μm. Topro3 marks cell nuclei. **(B)** Magnified images of the fornix and mammillothalamic tracts stained with NFL and Topro3 from serial coronal brain sections from P8 R1R3dKO and $Rtn1^{+/+}$; $Rtn3^{+/+}$ littermates. Fornix and mammillothalamic tracts are almost entirely missing in the P8 R1R3dKO sections. Scale bar indicates 50 μm. (**C**) Magnified image of NFL and ToPro3 staining in the cortex from P8 R1R3dKO and $Rtn1^{+/+}$; $Rtn3^{+/+}$ littermates. Reduced NFL signal is observed throughout the cortex at this stage. Overall size of the P8 R1R3dKo cortex also appears to be reduced. Individual images were manually stitched together to span the entirety of the cortex. White dotted lines indicate edges where images were stitched together. Scale bar indicates 50 μm. (**D**) MAP2 signal in the cortex from P8 R1R3dKO and $Rtn1^{+/+}$; $Rtn3^{+/+}$ littermates appears to be similar. Scale bar indicates 40 μm.

or abundance in tubular ER (see example in Fig. 5; arrows indicate tubular ER). In contrast, we noted reduction of length in synaptic active zone (Fig. 6A). Further quantification of active zone length showed reduction by ~27 ± 6% (Fig. 6B).

The shortened active zone length, as well as altered NFL of the SLM, suggests that RTN1 and RTN3 play a role on synaptic and axonal development. However, the mechanism for these phenomena does not appear to be related to axonal tubular ER morphology.

Rtn1 and *Rtn3* dual deficiency decreases proteins for synaptic functions

To investigate possible clues for altered axonal growth in R1R3dKO mouse brains, we conducted unbiased proteomic assays by comparing hippocampal lysates from three pairs of R1R3dKO and $Rtn1^{+/-}$;$Rtn3^{+/-}$ mice. Reduction of ~50% RTN1 and RTN3 protein levels were confirmed in this proteomic assay (Fig. 7A), which confirmed the validity of the assay. Of 1,701 identified proteins, only 16 proteins were found to be significantly different

Table 1. Differentially expressed proteins between R1R3dKO mice and control littermates: hippocampal protein lysates were processed for proteomic analysis by LC–MS methods. Means from each genotype reflected protein levels, and differences were subtracted mean of R1R3dKO from mean of control (Ctrl). *P*-value < 0.05, determined by Student *t*-test for each protein, was listed in the table ($n = 3$ samples per group)

Protein	P-value	Mean of R1R3dKO	Mean of Ctrl	Difference
Reticulon-1	0.000021	0.4302	1.126	−0.6960
Reticulon-3	0.000135	0.6523	1.153	−0.5004
Metaxin-1	0.001553	0.9782	1.162	−0.1840
Translocase of Inner Mitochondrial Membrane 44	0.005978	1.201	1.357	−0.1555
Staufen 2	0.008661	1.071	1.239	−0.1683
60s Ribosomal protein	0.008851	1.016	1.187	−0.1717
Ubiquitin Conjugating Enzyme E2 E3	0.013729	1.109	1.287	−0.1780
Nucleolar transcription factor 1	0.020010	1.095	1.235	−0.1401
Ring finger protein 214	0.021618	0.9138	1.113	−0.1994
Sideroflexin-1	0.023638	1.115	1.261	−0.1453
Cytoplasmic FMR1 Interacting Protein 1	0.029125	1.082	1.247	−0.1654
Plakoglobin	0.029154	0.9828	1.127	−0.1441
Cullin-4B	0.034428	1.020	1.154	−0.1344
Triokinase And FMN Cyclase	0.034529	0.9798	1.128	−0.1480
Phosphodiesterase 2A	0.034967	1.119	1.219	−0.1000
Fragile X Messenger Ribonucleoprotein 1	0.035488	1.085	1.265	−0.1801
Ubiquitin-Specific Peptidase 15	0.042023	0.9797	1.140	−0.1602

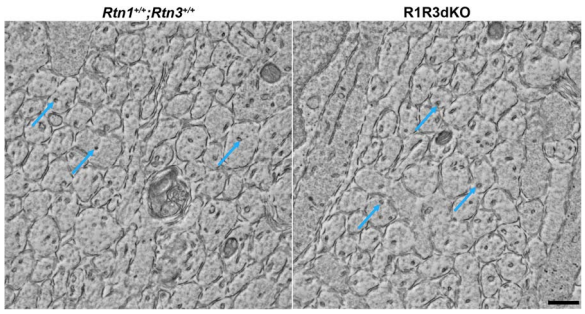

Figure 5. *Rtn1* and *Rtn3* dual deficiency does not alter axonal ER tubule morphology. Typical reduced osmium tetroxide EM images of SLM axons from P0 R1R3dKO and Ctrl littermate coronal sections are shown. Blue arrows specify the tubular ER. The shape and size of ER tubules are not distinguishably differed between P0 R1R3dKO and $Rtn1^{+/+}$;$Rtn3^{+/+}$ littermates. Scale bar, 500 nm.

[−log10(*P*-value) > 1.3] between R1R3dKO and $Rtn1^{+/-}$;$Rtn3^{+/-}$ littermates (see the volcano plot in Fig. 7A and summary in Table 1). Interestingly, NLF and NLM were not in this list of significantly altered proteins in R1R3dKO pups. Among the significantly downregulated proteins, FMR1 is recognized as fragile X messenger ribonucleoprotein 1, a risk gene for fragile X syndrome and the most common inherited form of intellectual disability. Mutations in these genes are causal factors for X-linked mental retardations (24). Cyfip1 is the cytoplasmic FMR1 interacting protein and regulates mRNA translational initiation via the 5'UTR (25). Staufen 2, known to bind RNA in the nucleus and to transport ribonucleoprotein particles from the nucleus to RNA granules in the cytoplasm (26), is known to form complexes with FMR1 and Cyfip1 to regulate synaptic bouton formation and glutamate receptor development (27).

Other noted downregulated proteins are Cullin 4B, PDE2A, TKFC and USP15. PDE2a is a phosphodiesterases, which are enzymes involved in the homeostasis of both cAMP and cGMP and have important roles in neural development and pathogenesis of diseases such as Down syndrome, fragile X syndrome, Rett syndrome and intellectual disability (28). Cullin 4B is a E3-ubiquitin ligase implicated in regulation of neural progenitor cell growth; genetic mutations of cullin-4B (*CUL4b*) cause a prevalent type of X-linked intellectual disability (XLID) in males (29–31). Genetic mutations of *CUL4b* are the most common causal factor of the XLID population, accounting for ∼3% patients (32). USP15 is a member of the ubiquitin-specific protease (USP) family of deubiquitinating enzymes, and mutations in USP15 have been linked to sporadic autism (33). Triokinase and FMN cyclase (TKFC) is involved in fructose metabolism, and deficiency of TKFC is associated with developmental delays in humans (34).

Hence, seven proteins of 16 downregulated proteins appear to be linked to intellectual development. These results suggest that RTN1 and RTN3 jointly regulate local translation of synaptic proteins and maintenance of synapses and are required for intellectual development.

Discussion

RTN1 and RTN3 are reticulons that are highly expressed by neurons (Supplementary Material, Fig. S5). The role of RTN3 in neurons has been linked to regulation of BACE1 activity and the formation of dystrophic neurites in Alzheimer's brains (35). The role of RTN1 in neuronal function was underinvestigated, although it was found in the SNARE protein complex (36). However, how these two proteins jointly play a role in rodent is not understood. In this study, we demonstrate that RTN1 and RTN3 are indispensable for mouse survival beyond P0. During mouse early development, deficiency of these two proteins will cause axonal defects, mainly in the perforant and temporammonic pathways. If dual deficient (R1R3dKO) mice would survive beyond P0, more striking axonal defects would be detected, indicating the critical role of these two proteins in the regulation of axonal growth. While defects in hippocampal development can cause neonatal lethality in the rodent (37), the observed defects in lung growth in R1R3dKO mice may be another reason for the neonatal lethality. H & E staining of lungs from R1R3dKO shows pathology for congested alveoli, similar to that in acute respiratory syndrome or pulmonary insufficiency (38,39). This is the first evidence that deficiency only two of four RTN members can cause mouse neonatal lethality, highlighting

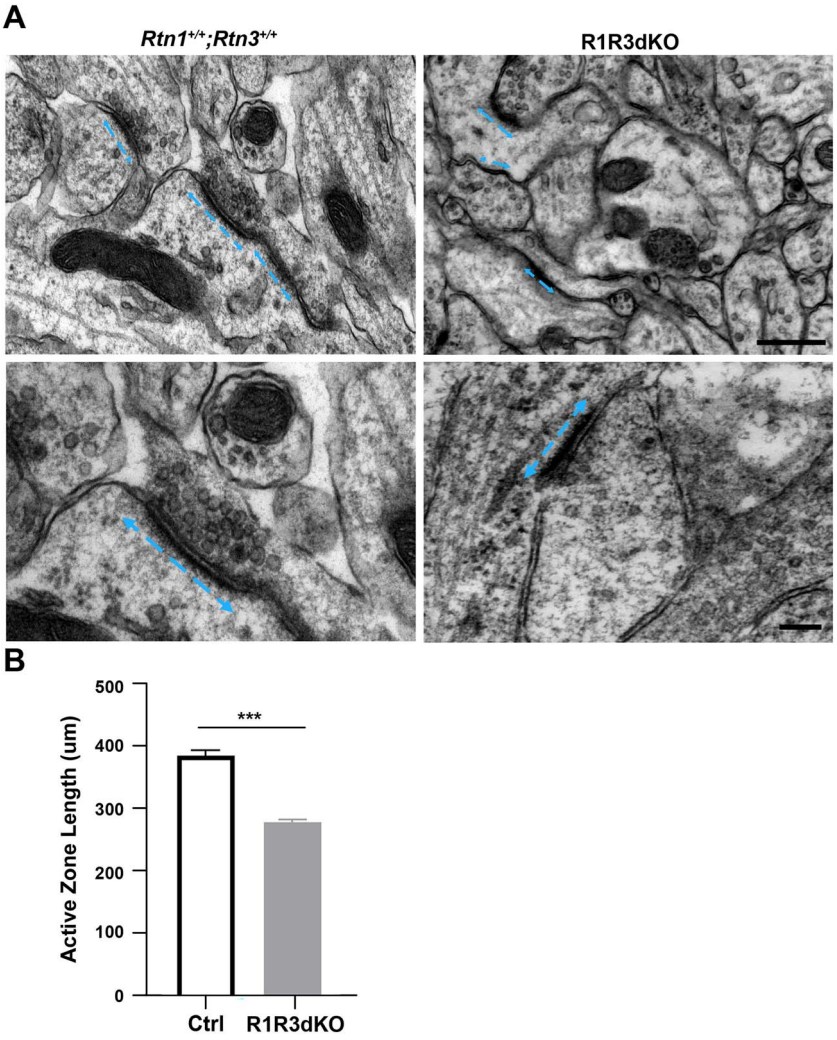

Figure 6. *Rtn1* and *Rtn3* dual deficiency reduces active zone length. (**A**) EM images of SLM synapses from P0 R1R3dKO and $Rtn1^{+/+};Rtn3^{+/+}$ littermate are represented in the top panel, with magnified images in the lower panel. Scale bar, 500 nm (top) and 100 nm (bottom). Length of active zones was highlighted by blue dashed lines. (**B**) Lengths (in nanometers) of active zone of SLM synapses were quantified ($n = 3$ mice, 60 active zones, One-way ANOVA with Holms–Sidak post-test of means, *** indicates P-value < 0.001).

the indispensable functions of RTNs in the rodent growth and neuronal functions.

The notable axonal defects in P0 R1R3dKO mouse brains appear to be restricted to the parahippocampal regions. This regional defect in axonal growth is likely related to the shared expression of these two RTNs in this area. By examining the publicly available spatial transcriptomic results (40), we noted that RTN protein family members, such as RTN1, RTN3, RTN4 and REEP2, have expression in both the SLM and ERC II layer of the temporammonic pathway (Supplementary Material, Fig. S6). Even though we observed the axonal defect, the ultrastructure of tubular ER in the hippocampus was not noticeably altered (Fig. 5), indicating that this dual deficiency is not sufficient to disrupt the ER structure. Likely, the presence of other tubular ER proteins will preserve the tubular ER structure in this region but not the function in axonal growth.

Since the joint functions of RTN1 and RTN3 are not compensated by other tubular RTNs or REEP proteins, the observed phenotypes of neonatal lethality and axonal growth defects in the parahippocampus are unlikely because of alteration in the tubular ER structure but rather altered expression of proteins regulated by these two proteins. Unbiased proteomic assays identified downregulation in expression of Staufen 2, Cyfip1, Cullin-4B, PDE2A and FMR1 (Fig. 7), which are known components in the fragile X mental retardation pathway. It has been demonstrated that the Staufen-2/FMRP ribonucleoprotein (RNP) complex is responsible for regulating post-synaptic gene expression as well as receptor endocytosis (41). Because these proteins are also localized to post-synaptic ER (42–44), it is highly likely that ER-localized reticulon proteins may interact with the Staufen-2/FMRP RNP complex, possibly via the coordinating ER/RNP contact site. These proteins have been shown to regulate structural and functional plasticity of glutamatergic axon terminals (25,27,28,41,43). Hence, the joint function of RTN1 and RTN3 is identified to control expression of genes important for the fragile X mental retardation pathway.

Consistent with the above proteomic results, we showed that active zone length in *Rtn1*/*Rtn3* dual deficient mice was significantly reduced (Fig. 6). How RTN1 and RTN3 regulate hippocampal synaptic density is not understood yet. One postulation is that this reduction is related to the reduction in neurofilament-mediated synaptic organization. We observed a lack of immunosignal for NFL, a common axonal cytoskeletal marker, in the distal portion of the temporammonic pathway with

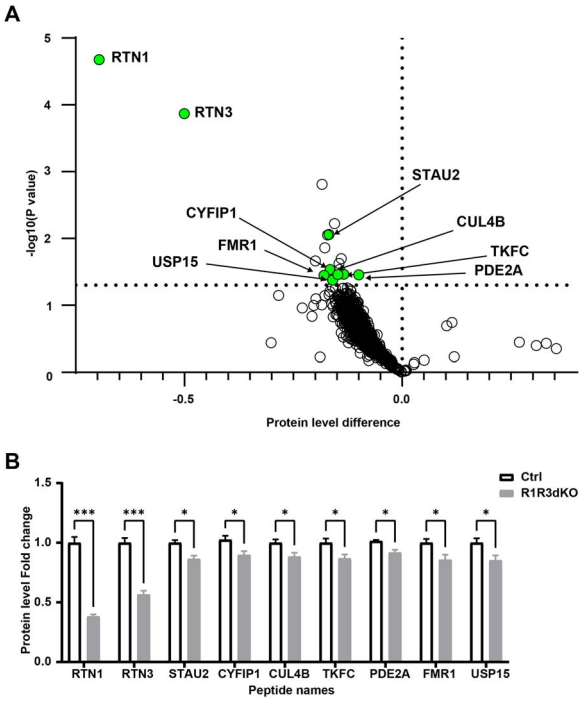

Figure 7. *Rtn1* and *Rtn3* dual deficiency reduces levels of multiple proteins associated with fragile X syndromes. (**A**) Volcano plot of differences in average protein levels and –log10 (*P*-value) from R1R3dKO hippocampi compared with Ctrl littermate hippocampi. Dotted *x*-line indicates –log10(*P*-value) = 1.3. Dotted *y*-line indicates a difference of 0. Labels and green dots highlight differentially expressed proteins linked to intellectual development. RTN1 and RTN3 are two proteins with ∼50% reduction, consistent with heterozygosity in both proteins. The *P*-value was determined by Student's *t*-test for each protein. $n = 3$ samples per group. (**B**) Bar graph compared changes of selected proteins between R1R3dKO and Ctrl mouse hippocampi. The *P*-value was determined by one-way ANOVA, with Tukey post-test ($n = 3$ samples per group. $^*P < 0.05$, $^{***}P < 0.001$).

origins in layer II of the entorhinal cortex projected to the SLM and angular bundle (Fig. 2). Neurofilaments (NFs) are best knowns as axonal structural components (46). However, recent studies have revealed that NFs can form a large protein complex along axons and synaptic terminals to regulate synaptic organization and functions (47,48). Loss of NFLs is sufficient to reduce axon caliber and synaptic activity (49). Intriguingly, the proteomic assay did not detect significant reduction of NFL and NFM (showed reduction by only 5–10%, not statistically significant for being listed in the volcano plot). The plausible reason is that levels of NFL and NFM are reduced only in the distal axonal part, and this reduction could not be reflected in the total NFL and NFM levels. Nevertheless, a small disruption of axonal NFL/NFM may cause defects in synaptic transmission, which is also reflected by the deficit of neuromuscular junction in the lung (Fig. 1D).

One mechanistic clue is the possible ER stress present in the R1R3dKO mice. We noted a reduction of a deubiquitinating enzyme, ubiquitin-specific peptidase 15 (USP15), in our proteomic assay. USP15 is crucial for RNA metabolism, and its inhibition will lead to mild and chronic ER stress (50). Elevated ER stress has been shown to be associated with the susceptibility of the fragile X syndrome as discussed above.

In summary, we describe multiple joint roles that RTN1 and RTN3 share on rodent neuronal development. By knocking out both proteins, we have revealed that RTN1 and RTN3 are critical for the organization of axonal cytoskeletal structure and possibly synaptic homeostasis. Tubular ER structural proteins in axons are important and indispensable in the mammalian systems, and their deficiency will lead to axonal loss and neurodegeneration.

Materials and Methods

Mouse strains and breeding strategy

Generation of *Rtn1*$^{-/-}$ *or Rtn3*$^{-/-}$ mice was previously described (21,22). Double knockout of *Rtn1* and *Rtn3* was achieved by breeding *Rtn1*$^{+/-}$;*Rtn3*$^{+/-}$ with *Rtn1*$^{+/-}$;*Rtn3*$^{+/-}$ mice. Resultant mice were confirmed by genotyping. Phenotypes of offspring were monitored, and neonatal lethality was noted in double KO mice but not in mice with deletion of single copies of both genes. Statistical data regarding lethality and body weights were recorded.

All experimental protocols were approved by the Institutional Animal Care and Use Committee of the Lerner Research Institute and University of Connecticut Health Center in compliance with the guidelines established by the Public Health Service Guide for the Care and Use of Laboratory animals.

Immunohistochemistry imaging

Immunohistochemistry was performed on mouse pup brains as previously described. Mice pups were perfused with PBS before brains were post-fixed in 4% PFA for 24 h. Brains were subsequently cryopreserved in 30% sucrose until equilibrated (∼2–3 days). Afterward, brains were embedded in the Optimal Cutting Temperature Compound (Fisher Scientific), cut serially to 12 μm by a freezing microtome (Thermo) and stored at −20°C until use. Slides were washed with phosphate buffer solution (PBS) for 3× 5 min before and between permeabilization with 0.3% Triton-X 100 and citric acid antigen retrieval. Tissues were then blocked with 5% normal goat serum and incubated with primary antibody (see antibody list) for 2 h at 37°C and overnight 4°C. Afterward, tissues were incubated with compatible fluorescent secondary antibodies for 2 h at 37°C, before mounting in Vectashield mounting media and coverslipped. Certain sections were counterstained with ToPro-3 (ThermoFisher). For gross histology, certain sections were Nissl-stained.

Diaphragms were extracted from P0 mice and fixed in 4% PFA according to the published protocol (51). Diaphragms were treated as floating sections and were washed, permeabilized and blocked in the same manner as brain sections. Subsequently diaphragms were incubated in AChR staining α-bungarotoxin conjugated to Alexa 488 fluorophore (ThermoFisher) at room temperature for 4 h. Diaphragms were carefully placed to avoid wrinkles onto slides before mounting with Vectashield and cover-slipped. Lung sections samples were stained with H & E.

For whole brain images, Keyence BZX-810 fluorescent microscope was used for mosaic imaging and stitching. Other images were captured with either a Leica TCS-SP8-AOBS or Zeiss LSM 800 Confocal microscope.

Imaging analysis and quantification

Images were analyzed with ImageJ software. For AChR puncta density, puncta within the bounds of the normal phrenic nerve end plate were counted manually and normalized to the end-plate area. Three diaphragms were analyzed from either R1R3dKO or control groups. Quantification of the NFL fluorescent signal was achieved by measuring raw integrated density within the bound of the SLM. Sagittal sections 0.8, 1.6 and 2.4 mm from midline were used for analysis. Six mice from either R1R3dKO or control groups were used.

Representative 3D visualization of NFL fluorescent signaling was performed using the software Reconstruct. Briefly, 12 whole

brain sagittal sections with 120 μM intervals were selected from a range of section 0.8 to 2.4 mm from midline. Whole brain (teal volume), hippocampus (red volume) and NFL signal of the SLM (green volume) were then traced and spaced according to serial interval.

Electron microscopy

Electron microscopy of P0 mice was performed twice, once at the Cleveland Clinic Foundation and once at the University of Connecticut Health Center Electron Microscopy Cores as previously described (52). Briefly, P0 mice were perfused intracardially with ∼10 ml of 0.1 m sodium cacodylate buffer containing 4% paraformaldehyde and 2.5% glutaraldehyde, pH 7.4. The left and right extracted brains were fixed overnight with 0.1 m sodium cacodylate buffer containing 4% paraformaldehyde and 2.5% glutaraldehyde. After washing three times with 0.1 M sodium cacodylate, the samples were placed in 0.1% tannic acid for 30 min and then washed with sodium cacodylate solution. Next, the samples were sequentially processed by 2 h incubation with 2% osmium tetroxide/potassium ferrocyanide on ice, 20 min treatment with freshly prepared 1% thiocarbohydrazide at 60°C and 1 h incubation with 2% osmium tetroxide solution on a rotor at room temperature. The samples were then placed in new vials, washed three times with distilled water and placed in saturated uranyl acetate solution overnight at 4°C. The following day, samples were washed three times with distilled water and finally stained with lead aspartate solution (prepared by dissolving 0.066 g of lead nitrate in 10 ml 0.03 m aspartic acid, pH 5.5) at 60°C for 30 min and washed again with distilled water three times. The samples were then dehydrated by dipping the samples twice (5 min each) in a gradient series of freshly prepared solutions of 50, 75, 85, 95 and 100% ethanol and finally by placing in anhydrous acetone for 10 min at room temperature. The samples were then transferred to freshly made 50% Epon resin in propylene prepared by mixing 5 ml propylene with 5 ml of 100% Epon resin formulated as 10 ml EMBed-812, 8 ml dodecenyl succinic anhydride, 4 ml methyl-5-norbornene-2,3-dicarboxylic anhydride and 0.4 ml 2,4,6-tri (dimethylaminomethyl)-phenol. After incubating for 2 h at room temperature in 50% Epon, the samples were transferred to 100% Epon and rotated for 90 min. Finally, the samples were placed into molds and fresh Epon resin was poured and kept at 60°C for 2 days for polymerization and solidification.

Sample blocks of 0.5 × 0.5 × 0.5 mm size for each hippocampal tissue was prepared by trimming the resin using a razor blade. Each sample block was mounted on a pin and was then set on the stage of a Zeiss Sigma VP scanning electron microscope equipped with a Gatan 3View in-chamber ultramicrotome and a low-kilovolt backscattered electron detector. The diamond knife of the microscope was set to make ∼500 sections at a thickness of 70 nm. Images were generated at 2.0–2.25 kV under standard vacuum conditions using an aperture set at 30 μm and captured at 5 nm/pixel resolution (×5000 magnification). Active zone length from 60 synapses in SLM was recorded from three mice for each group using ImageJ.

Liquid chromatography mass spectrometry and analysis

Liquid chromatography mass spectrometry and analysis was performed on three R1R3dKO and three *Rtn1*$^{+/-}$;*Rtn3*$^{+/-}$ brains as per methodology detailed in (53).

Sample preparation

Sample lysis buffer (2% SDS, 0.5 M tetraethyl-ammonium bicarbonate (TEAB), protease inhibitor cocktail) were added to each brain tissue and then homogenized by TissueLyser LT (Qiagen, Valencia, CA). Tissue homogenates were centrifuged at 17 000 × *g*, for 20 min at 4°C. The supernatant was transferred into a new vial for protein concentration measurement by the BCA assay. Preparation of tryptic peptides for TMT 10-plex labeling was carried out according to the manufacturer's instructions. Briefly, 100 μg protein from each sample was transferred into a new vial and adjusted to a final volume of 100 μl with TEAB and reduced with tris (2-carboxyethyl) phosphine (TCEP) at 55°C for 1 h and then alkylated with iodoacetamide for 30 min in the dark. Methanol–chloroform precipitation was performed prior to protease digestion. In brief, four parts methanol was added to each sample and vortexed; then, one part chloroform was added to the sample and vortexed, and three parts water were added to the sample and vortexed. The sample was centrifuged at 14 000 × *g* for 4 min at room temperature and the aqueous phase was removed. The organic phases with protein precipitate at the surface was subsequently washed twice with four parts methanol and centrifuged with the supernatant being removed subsequently. After air-drying, precipitated protein pellets were resuspended with 100 μl of 50 mM TEAB and digested with trypsin overnight at 37°C.

Tryptic digested peptides from brain samples were labeled with TMT 10-plex reagents (Thermo Fisher) according to manufacturer's instructions and analyzed simultaneously. Briefly, the TMT reagents (0.8 mg) were dissolved in 41 μl of anhydrous acetonitrile. Aliquots of samples were incubated with TMT reagents for 1 h at room temperature. The reactions were quenched by 8 μl of 5% hydroxylamine solution and reacted for 15 min. The combined TMT labeled samples were dried under SpeedVac and then reconstituted by dilute trifluoroacetic acid solution followed by desalting by the Oasis HLB 96-well μElution plate (Waters) prior to LC–MS/MS analysis.

LC–MS/MS

LC–MS/MS was performed on a QExactive Orbitrap Mass Spectrometer (ThermoFisher Scientific) coupled with a Dionex Ultimate 3000 HPLC system equipped with a nano-ESI ion source. The TMT-labeled peptides were separated on a C18 reverse-phase capillary column (PepMap, 75 μm × 150 mm, ThermoFisher) with linear gradients of 2–35% acetonitrile in 0.1% formic acid, at a constant flow rate of 300 nl/min for 220 min. The instrument was operated in the positive-ion mode with the ESI spray voltage set at 1.8 kV. A full-scan MS spectrum (300–1800 *m/z*) was acquired in the Orbitrap at a mass resolution of 70 000 with an automatic gain control target (AGC) of 3e6. Fifteen peptide ions showing the most intense signal from each scan were selected for higher energy collision-induced dissociation (HCD)-MS/MS analysis (normalized collision energy 32) in the Orbitrap at a mass resolution of 35 000 and an AGC value of 1e5. Maximal filling times were 100 ms in full scans and 120 ms (HCD) for the MS/MS scans. Ions with unassigned charge states and singly charged species were rejected. The dynamic exclusion was set to 50 s and a relative mass window of 10 ppm. The data were acquired using Thermo Xcalibur 3.0.63. The phosphopeptides were analyzed under the same conditions as above, other than the separation that was done with linear gradients of 1–30% acetonitrile in 0.1% formic acid, and full-scan MS ranging 300–2000 *m/z* with NCE at 25.

Protein identification and quantification

Raw data were processed using Proteome Discoverer (Version 2.1, Thermo Fisher Scientific). Data were searched against the

Mus musculus Universal Protein Resource sequence database (UniProt, August, 2013). The searches were performed with the following guidelines: Trypsin digestion with two missed cleavage allowed; fixed modification, carbamidomethyl of cysteine; variable modification, oxidation of methionine, TMT 10plex (peptide labeled) for N terminus and Lys; MS tolerance, 5 ppm; MS/MS tolerance, 0.02 Da; false discovery rate (FDR) at peptide and protein levels, <0.01; and required peptide length, ≥ 6 amino acids. Phosphorylation of serine, threonine and tyrosine was defined as variable modification. Protein grouping was enabled, meaning if one protein were equal to or completely contained within the set of peptides of another protein, these two proteins were put into the same protein group. At least one unique peptide per protein group was required for identifying proteins. The relative protein abundance ratios (fold changes) between R1R3dKO and R1R3dKO and $Rtn1^{+/-}$;$Rtn3^{+/-}$ groups were calculated. The changes in protein levels were considered significant if differences of means were >1.1 (upregulated) or <0.9 (downregulated), and the *P*-value was <0.05 in two independent experiments.

Genotyping primers

Primer target	Sequence (5′->3′)
RTN1KO557-F	GAAAAGGTGTGGGCTTTTGA
RTN1KO557-R	GCTTGGCTGGAGGTAAACTC
RTN3KO491-F′	ACACTCTACCTGCACTGGACTT
RTN3KO491-R	GCCAGAGGCCACTTGTGTAG

Antibody list used for the study

Antibody Name	Catalog No.	RRID:	Manufacturer
Ki67	19972-1-AP		ProteinTech
NeuN	MAB337	AB_2313673	Millipore
Neuofilament Medium Chain (NFM)	AB9568	AB_11213875	Millipore
Neurofilament Medium Chain (NLM)	2H3-s	AB_1542506	DSHB
P73	AB40658	AB_776999	Abcam
Reelin	MAB5364	AB_2313695	Millipore
SMI31	11476	AB_10122491	BioLegend

Statistical analysis

Bar graph results are expressed as mean ± SD. The statistical analyses were performed using GraphPad Prism 6.0 software (GraphPad Software, San Diego). Student's *t*-tests were used to compare between two groups. Two-way ANOVAs were used to compare multiple groups, post-test of Sidak, Tukey or Bonferroni was used to compare between different groups. Differences with $^{*}P<0.05$, $^{**}P<0.01$ and $^{***}P<0.001$ were considered significant.

Supplementary Material

Supplementary Material is available at *HMG* online.

Acknowledgements and Funding

We are grateful for Dr. Mark Terasaki for his support to the analysis of the tubular endoplasmic reticulum. Cleveland Clinic and University of Connecticut Health Center Electron Microscopy Core provided electron microscopy services. R.Y. is supported by grants RF1AG058261, AG025493, NS074256 and AG046929 from the National Institutes of Health. R.Y.'s laboratory is also supported by the Cure Alzheimer's Fund.

Conflict of Interest statement. None declared.

Ethical Approval and Consent to Participate

All experimental protocols were approved by the Institutional Animal Care and Use Committee of the University of Connecticut, School of Medicine in compliance with the guidelines established by the Public Health Service Guide for the Care and Use of Laboratory Animals.

Consent for Publication

All authors have read and approved the final manuscript.

Availability of Supporting Data

All original data presented in the paper will be made available for reviews when needed. Research materials will be also made available when it is required.

Authors' Contributions

J.Z. designed and conducted experiments and wrote the draft. Q.S., Y.G. and W.H. conducted partial experiments. X.H. helped in data analysis. W.X. conducted proteomic experiments. R.Y. supervised the project and wrote the manuscript.

Data Availability

All data is provided in figures or supplementary figures.

References

1. Shibata, Y., Hu, J., Kozlov, M.M. and Rapoport, T.A. (2009) Mechanisms shaping the membranes of cellular organelles. *Annu. Rev. Cell Dev. Biol.*, **25**, 329–354.
2. Goyal, U. and Blackstone, C. (2013) Untangling the web: mechanisms underlying ER network formation. *Biochim. Biophys. Acta*, **1833**, 2492–2498.
3. English, A.R. and Voeltz, G.K. (2013) Endoplasmic reticulum structure and interconnections with other organelles. *Cold Spring Harb. Perspect. Biol.*, **5**, a013227.
4. Stefano, G., Hawes, C. and Brandizzi, F. (2014) ER - the key to the highway. *Curr. Opin. Plant Biol.*, **22**, 30–38.
5. Nziengui, H. and Schoefs, B. (2008) Functions of reticulons in plants: what we can learn from animals and yeasts. *Cell. Mol. Life Sci.*, **66**, 584–595.
6. Oertle, T. and Schwab, M.E. (2003) Nogo and its paRTNers. *Trends Cell Biol.*, **13**, 187–194.
7. Voeltz, G.K., Prinz, W.A., Shibata, Y., Rist, J.M. and Rapoport, T.A. (2006) A class of membrane proteins shaping the tubular endoplasmic reticulum. *Cell*, **124**, 573–586.
8. O'Sullivan, N.C., Jahn, T.R., Reid, E. and O'Kane, C.J. (2012) Reticulon-like-1, the drosophila orthologue of the hereditary spastic paraplegia gene reticulon 2, is required for organization of endoplasmic reticulum and of distal motor axons. *Hum. Mol. Genet.*, **21**, 3356–3365.

9. Yalçın, B., Zhao, L., Stofanko, M., O'Sullivan, N.C., Kang, Z.H., Roost, A., Thomas, M.R., Zaessinger, S., Blard, O., Patto, A.L. *et al.* (2017) Modeling of axonal endoplasmic reticulum network by spastic paraplegia proteins. *eLife*, **6**, e23882.
10. Yang, Y.S. and Strittmatter, S.M. (2007) The reticulons: a family of proteins with diverse functions. *Genome Biol.*, **8**, 234.
11. Chiurchiu, V., Maccarrone, M. and Orlacchio, A. (2014) The role of reticulons in neurodegenerative diseases. *NeuroMolecular Med.*, **16**, 3–15.
12. Park, S.H., Zhu, P.P., Parker, R.L. and Blackstone, C. (2010) Hereditary spastic paraplegia proteins REEP1, spastin, and atlastin-1 coordinate microtubule interactions with the tubular ER network. *J. Clin. Invest.*, **120**, 1097–1110.
13. Chen, M.S., Huber, A.B., van der Haar, M.E., Frank, M., Schnell, L., Spillmann, A.A., Christ, F. and Schwab, M.E. (2000) Nogo-a is a myelin-associated neurite outgrowth inhibitor and an antigen for monoclonal antibody IN-1. *Nature*, **403**, 434–439.
14. GrandPre, T., Nakamura, F., Vartanian, T. and Strittmatter, S.M. (2000) Identification of the Nogo inhibitor of axon regeneration as a Reticulon protein. *Nature*, **403**, 439–444.
15. Woolf, C.J. (2003) No Nogo: now where to go? *Neuron*, **38**, 153–156.
16. Acevedo, L., Yu, J., Erdjument-Bromage, H., Miao, R.Q., Kim, J.E., Fulton, D., Tempst, P., Strittmatter, S.M. and Sessa, W.C. (2004) A new role for Nogo as a regulator of vascular remodeling. *Nat. Med.*, **10**, 382–388.
17. Gao, L., Utsumi, T., Tashiro, K., Liu, B., Zhang, D., Swenson, E.S. and Iwakiri, Y. (2013) Reticulon 4B (Nogo-B) facilitates hepatocyte proliferation and liver regeneration in mice. *Hepatology*, **57**, 1992–2003.
18. He, W., Lu, Y., Qahwash, I., Hu, X.Y., Chang, A. and Yan, R. (2004) Reticulon family members modulate BACE1 activity and amyloid-beta peptide generation. *Nat. Med.*, **10**, 959–965.
19. He, W., Hu, X., Shi, Q., Zhou, X., Lu, Y., Fisher, C. and Yan, R. (2006) Mapping of interaction domains mediating binding between BACE1 and RTN/Nogo proteins. *J. Mol. Biol.*, **363**, 625–634.
20. Sharoar, M.G., Shi, Q., Ge, Y., He, W., Hu, X., Perry, G., Zhu, X. and Yan, R. (2016) Dysfunctional tubular endoplasmic reticulum constitutes a pathological feature of Alzheimer's disease. *Mol. Psychiatry*, **21**, 1263–1271.
21. Shi, Q., Ge, Y., He, W., Hu, X. and Yan, R. (2017) RTN1 and RTN3 protein are differentially associated with senile plaques in Alzheimer's brains. *Sci. Rep.*, **7**, 6145.
22. Shi, Q., Ge, Y., Sharoar, M.G., He, W., Xiang, R., Zhang, Z., Hu, X. and Yan, R. (2014) Impact of RTN3 deficiency on expression of BACE1 and amyloid deposition. *J. Neurosci.*, **34**, 13954–13962.
23. Terasaki, M., Shemesh, T., Kasthuri, N., Klemm, R.W., Schalek, R., Hayworth, K.J., Hand, A.R., Yankova, M., Huber, G., Lichtman, J.W., Rapoport, T.A. and Kozlov, M.M. (2013) Stacked endoplasmic reticulum sheets are connected by helicoidal membrane motifs. *Cell*, **154**, 285–296.
24. Wiseman, S. (2022) A fragile imbalance. *Nat. Neurosci.*, **25**, 838.
25. Biembengut, Í.V., Silva, I.L.Z., de Souza, T.D.A.C.B. and Shigunov, P. (2021) Cytoplasmic FMR1 interacting protein (CYFIP) family members and their function in neural development and disorders. *Mol. Biol. Rep.*, **48**, 6131–6143.
26. Miki, T., Takano, K. and Yoneda, Y. (2005) The role of mammalian Staufen on mRNA traffic: a view from its nucleocytoplasmic shuttling function. *Cell Struct. Funct.*, **30**, 51–56.
27. Song, C., Leahy, S.N., Rushton, E.M. and Broadie, K. (2022) RNA-binding FMRP and Staufen sequentially regulate the coracle scaffold to control synaptic glutamate receptor and Bouton development. *Development*, **149**.
28. Delhaye, S. and Bardoni, B. (2021) Role of phosphodiesterases in the pathophysiology of neurodevelopmental disorders. *Mol. Psychiatry*, **26**, 4570–4582.
29. Liu, H.C., Enikolopov, G. and Chen, Y. (2012) Cul4B regulates neural progenitor cell growth. *BMC Neurosci.*, **13**, 112.
30. Zhao, Y. and Sun, Y. (2012) CUL4B ubiquitin ligase in mouse development: a model for human X-linked mental retardation syndrome? *Cell Res.*, **22**, 1224–1226.
31. Zou, Y., Liu, Q., Chen, B., Zhang, X., Guo, C., Zhou, H., Li, J., Gao, G., Guo, Y., Yan, C. *et al.* (2007) Mutation in CUL4B, which encodes a member of cullin-RING ubiquitin ligase complex, causes X-linked mental retardation. *Am. J. Hum. Genet.*, **80**, 561–566.
32. Tarpey, P.S., Raymond, F.L., O'Meara, S., Edkins, S., Teague, J., Butler, A., Dicks, E., Stevens, C., Tofts, C., Avis, T. *et al.* (2007) Mutations in CUL4B, which encodes a ubiquitin E3 ligase subunit, cause an X-linked mental retardation syndrome associated with aggressive outbursts, seizures, relative macrocephaly, central obesity, hypogonadism, pes cavus, and tremor. *Am. J. Hum. Genet.*, **80**, 345–352.
33. O'Roak, B.J., Vives, L., Fu, W., Egertson, J.D., Stanaway, I.B., Phelps, I.G., Carvill, G., Kumar, A., Lee, C., Ankenman, K. *et al.* (2012) Multiplex targeted sequencing identifies recurrently mutated genes in autism spectrum disorders. *Science*, **338**, 1619–22.
34. Wortmann, S.B., Meunier, B., Mestek-Boukhibar, L., van den Broek, F., Maldonado, E.M., Clement, E., Weghuber, D., Spenger, J., Jaros, Z., Taha, F. *et al.* (2020) Bi-allelic Variants in TKFC encoding triokinase/FMN cyclase are associated with cataracts and multisystem disease. *Am. J. Hum. Genet.*, **106**, 256–263.
35. Sharoar, M.G. and Yan, R. (2017) Effects of altered RTN3 expression on BACE1 activity and Alzheimer's neuritic plaques. *Rev. Neurosci.*, **28**, 145–154.
36. Steiner, P., Kulangara, K., Sarria, J.C.F., Glauser, L., Regazzi, R. and Hirling, H. (2004) Reticulon 1-C/neuroendocrine-specific protein-C interacts with SNARE proteins. *J. Neurochem.*, **89**, 569–580.
37. Corbo, J.C., Deuel, T.A., Long, J.M., LaPorte, P., Tsai, E., Wynshaw-Boris, A. and Walsh, C.A. (2002) Doublecortin is required in mice for lamination of the hippocampus but not the neocortex. *J. Neurosci.*, **22**, 7548–7557.
38. Jin, J., Li, Y., Ren, J., Man Lam, S., Zhang, Y., Hou, Y., Zhang, X., Xu, R., Shui, G. and Ma, R.Z. (2016) Neonatal respiratory failure with retarded perinatal lung maturation in mice caused by reticulocalbin 3 disruption. *Am. J. Respir. Cell Mol. Biol.*, **54**, 410–423.
39. Ikeda, H., Shiojima, I., Oka, T., Yoshida, M., Maemura, K., Walsh, K., Igarashi, T. and Komuro, I. (2011) Increased Akt-mTOR signaling in lung epithelium is associated with respiratory distress syndrome in mice. *Mol. Cell. Biol.*, **31**, 1054–1065.
40. Ortiz, C., Navarro, J.F., Jurek, A., Märtin, A., Lundeberg, J. and Meletis, K. (2020) Molecular atlas of the adult mouse brain. *Sci. Adv.*, **6**, eabb3446.
41. Heraud-Farlow, J.E. and Kiebler, M.A. (2014) The multifunctional Staufen proteins: conserved roles from neurogenesis to synaptic plasticity. *Trends Neurosci.*, **37**, 470–479.
42. Kiebler, M.A., Hemraj, I., Verkade, P., Köhrmann, M., Fortes, P., Marión, R.M., Ortín, J. and Dotti, C.G. (1999) The mammalian Staufen protein localizes to the somatodendritic domain of cultured hippocampal neurons: implications for its involvement in mRNA transport. *J. Neurosci.*, **19**, 288–297.
43. Marfull-Oromí, P., Onishi, K., Han, X., Yates, J.R., 3rd and Zou, Y. (2023) The fragile X messenger ribonucleoprotein 1 participates in axon guidance mediated by the Wnt/planar cell polarity pathway. *Neuroscience*, **508**, 76–86.

44. Monday, H.R., Kharod, S.C., Yoon, Y.J., Singer, R.H. and Castillo, P.E. (2022) Presynaptic FMRP and local protein synthesis support structural and functional plasticity of glutamatergic axon terminals. *Neuron*, **110**, 2588–2606.e6.
45. Yu, Z., Fan, D., Gui, B., Shi, L., Xuan, C., Shan, L., Wang, Q., Shang, Y. and Wang, Y. (2012) Neurodegeneration-associated TDP-43 interacts with fragile X mental retardation protein (FMRP)/Staufen (STAU1) and regulates SIRT1 expression in neuronal cells. *J. Biol. Chem.*, **287**, 22560–22572.
46. Lee, M.K. and Cleveland, D.W. (1996) Neuronal intermediate filaments. *Annu. Rev. Neurosci.*, **19**, 187–217.
47. Bucher, M., Fanutza, T. and Mikhaylova, M. (2020) Cytoskeletal makeup of the synapse: shaft versus spine. *Cytoskeleton (Hoboken)*, **77**, 55–64.
48. Yuan, A., Rao, M.V., Veeranna, R.A. and Nixon, R.A. (2017) Nixon, Neurofilaments and Neurofilament proteins in health and disease. *Cold Spring Harb. Perspect. Biol.*, **9**, a018309.
49. Sainio, M.T., Rasila, T., Molchanova, S.M., Järvilehto, J., Torregrosa-Muñumer, R., Harjuhaahto, S., Pennonen, J., Huber, N., Herukka, S.K., Haapasalo, A. *et al.* (2021) Neurofilament light regulates axon Caliber, synaptic activity, and organelle trafficking in cultured human motor neurons. *Front. Cell Dev. Biol.*, **9**, 820105.
50. Kim, J., Nakamura, J., Hamada, C., Taketomi, T., Yano, S., Okajima, T., Kashiwabara, S.I., Baba, T., Sato, B., Chiba, T. and Tsuruta, F. (2020) USP15 Deubiquitinates TUT1 associated with RNA metabolism and maintains cerebellar homeostasis. *Mol. Cell. Biol.*, **40**, e00098–20.
51. Wu, H. and Mei, L. (2013) Morphological analysis of neuromuscular junctions by immunofluorescent staining of whole-mount mouse diaphragms. *Methods Mol. Biol.*, **1018**, 277–285.
52. Sharoar, M.G., Hu, X., Ma, X.M., Zhu, X. and Yan, R. (2019) Sequential formation of different layers of dystrophic neurites in Alzheimer's brains. *Mol. Psychiatry*, **24**, 1369–1382.
53. Chen, M. and Xia, W. (2020) Proteomic profiling of plasma and brain tissue from Alzheimer's disease patients reveals candidate network of plasma biomarkers. *J. Alzheimers Dis.*, **76**, 349–368.